JOURNAL OF GEOPHYSICAL RESEARCH, VOL. 113, C04015, doi:10.1029/2007JC004256, 2008

Spatial and interannual variability in mesoscale circulation in the northern California Current System

Julie E. Keister[1] and P. Ted Strub[1]

Received 31 March 2007; revised 16 October 2007; accepted 5 December 2007; published 12 April 2008.

[1] We used wavelet analyses of sea surface height (SSH) from >13 years of satellite altimeter data to characterize the variability in mesoscale circulation in the northern California Current (35°N–49°N) and explore the mechanisms of variability. We defined "mesoscale" circulation as features, such as eddies and filaments, which have 50- to 300-km length scales and 4- to 18-week temporal scales. Fluctuations in SSH caused by such features were reflected in wavelet analyses as power (energy). Spatial and interannual variation in mesoscale energy was high. Energy was highest at ~38°N, decreasing to the north and south. Between ~43°N and 48°N, energy was low. Zonally, mesoscale energy was highest between ~125°W and 129°W at latitudes south of 44°N; very little power occurred in the deep ocean west of 130°W. Energy peaked during summer/fall in most years. The primary climate signals were suppressed energy during La Niña and cold years and increased energy during El Niño events. Energy was not strongly linked to upwelling winds, but did correspond to climate indices, indicating that basin-scale processes play a role in controlling mesoscale circulation. We hypothesize that climate affects mesoscale energy through changes in both potential and kinetic energy in the form of density gradients and coastal upwelling winds. The relationship between mesoscale circulation and climate was complex: no single climate, transport, or upwelling index explained the variability. These results are relevant to ecosystem dynamics and the global carbon cycle because mesoscale circulation features deliver nutrient-rich water and coastal organisms from productive upwelling areas to the deep sea.

Citation: Keister, J. E., and P. T. Strub (2008), Spatial and interannual variability in mesoscale circulation in the northern California Current System, *J. Geophys. Res.*, *113*, C04015, doi:10.1029/2007JC004256.

1. Introduction

[2] In coastal upwelling ecosystems, offshore advection is an important factor controlling populations of coastal organisms. Typically, wind-driven Ekman transport has been considered the dominant mechanism of cross-shelf flow during upwelling, but more recently circulation features such as "squirts," filaments, and eddies are recognized as being important contributors to such transport. One such feature may transport as much mass offshore as all of the Ekman transport forced by 10 m s^{-1} (20 kt) winds along ~1000 km of coastline [*Kosro and Huyer*, 1986]. Such features, particularly cold-core filaments, are common in some areas of the California Current System (CCS) and may persist several months, potentially delivering huge amounts of coastal water and the associated biology to the deep ocean [*Brink et al.*, 2000; *Huyer et al.*, 1998; *Mackas et al.*, 1991].

[3] In terms of primary production and fisheries yield, the California Current (CC) is one of the highly productive global Eastern Boundary Current (EBC) upwelling ecosystems [*Barber and Smith*, 1981]. The system is characterized by temporally and spatially variable physical forcings, seasonal wind-driven upwelling in the northern CCS, and year-round upwelling in the southern CCS. The phytoplankton and zooplankton response to upwelling supports high production of upper trophic levels. The general circulation in the CCS includes energetic eddies, filaments, and meanders of the alongshore upwelling jet.

[4] Many publications have described mesoscale circulation off the U.S. Pacific coast during specific cruises or over a few years. Eddy kinetic energy and individual circulation features in the CCS have been studied from shipboard observations [*Barth et al.*, 2005; *Kosro et al.*, 1991; *Kosro and Huyer*, 1986], using satellite altimetry [e.g., *Kelly et al.*, 1998; *Strub and James*, 2000, 2002a], moorings [*Chereskin et al.*, 2000], satellite radiometers [*Castelao et al.*, 2006; *Legaard and Thomas*, 2006], surface drifters [*Brink et al.*, 2000], and subsurface floats [*Collins et al.*, 2004]. From the above studies we know that mesoscale variability peaks seasonally in late summer/fall, increases in areas of complex bottom topography (particularly in the vicinity of Cape Blanco, Cape Mendocino, and Pt. Arena) and that mesoscale features can carry energy and water mass from nearshore to offshore.

[5] As part of the U.S. Global Ocean Ecosystems Dynamics Northeast Pacific program (GLOBEC NEP) we are

[1]College of Oceanic and Atmospheric Sciences, Oregon State University, Corvallis, Oregon, USA.

0148-0227/08/2007JC004256$09.00

studying how changing climate, through its impacts on local forcings (e.g., upwelling), affects variability in mesoscale circulation in the northern California Current System and how that variability cascades through the ecosystem. One of the goals of the GLOBEC NEP program is to examine the role of mesoscale variability in controlling zooplankton distribution and retention/loss from coastal areas. Mesoscale circulation in the northern CCS is believed to primarily derive its energy from baroclinic instabilities in the alongshore-flowing, surface-intensified, coastal upwelling jet [*Batteen*, 1997; *Haidvogel et al.*, 1991; *Marchesiello et al.*, 2003; *Narimousa and Maxworthy*, 1989]. The upwelling jet draws its energy from alongshore, upwelling-favorable (equatorward) winds [*Batteen*, 1997] which are driven by basin-scale sea level pressure and temperature gradients [*Batteen*, 1997; *Schwing et al.*, 2002a]. Thus, because climate variability is associated with large-scale changes in winds and temperatures [*Bakun*, 1990; *Miller and Schneider*, 2000; *Schwing et al.*, 2002a; *Snyder et al.*, 2003], temporal variability in mesoscale circulation in the CCS is likely to be affected by climate. We hypothesize that interannual variability in the timing and intensity of mesoscale circulation is related to the timing of the transition to northerly, upwelling-favorable winds in spring, the cumulative intensity of northerly winds through the upwelling season, the southward transport into the CCS, and cross-shelf density gradients.

[6] Changes in circulation patterns may impact the abundance and availability of prey to ecologically and commercially important fish populations and affect cross-shelf delivery of production to the deep sea. Understanding the links between climate, mesoscale circulation, and biological patterns will require quantitative measures of the variability of the physics and the biology. Several indices of climate relevant to the northeast Pacific have been developed, for example, the Pacific Decadal Oscillation (PDO), the Multivariate ENSO Index (MEI), the Northern Oscillation Index (NOI), etc., and have been shown to correlate with biological variability [e.g., *Hooff and Peterson*, 2006; *Mantua et al.*, 1997; *Schwing et al.*, 2002b]. Changes in mesoscale circulation likely influence variability in primary production [e.g., *Henson and Thomas*, 2007b] and higher trophic levels. However, at present we lack a quantitative evaluation of the interannual variability in mesoscale activity in the NEP and its role in ecosystem dynamics.

[7] We use satellite altimetry to study the spatial and temporal variability in mesoscale activity in the northern CCS as a step toward understanding how such variability may impact the productivity of the system on intra and interannual timescales. This study expands upon previous studies of mesoscale activity in the CCS [*Chereskin et al.*, 2000; *Kelly et al.*, 1998; *Strub and James*, 2000] by explicitly examining interannual variability over >13 years (1992–2006). During this period, substantial variability in forcing, including a strong El Niño and La Niña occurred, which allows us to examine climate effects on mesoscale circulation.

[8] Following a description of our study area (section 2) and data (section 3), we give a brief overview of our statistical method, wavelet transforms, in section 4. We provide an overview of the spatial and temporal variability in the northern CCS using sea level observations and wavelet transforms of the data in section 5, focusing on variability in mesoscale circulation. Therein, we include a detailed comparison of wavelet spectra from two locations as an introduction to the interpretation of wavelet results. In section 6, we use observations of current transport, upwelling indices, and hydrographic data to address the question of how mesoscale activity responds to local forcings. Noting that interannual patterns of mesoscale energy do not closely match patterns of local forcings, we then investigate mechanisms through which basin-scale forcings may control mesoscale activity.

2. Study Area

[9] Our study area is the northern California Current from 35°N to 49°N, 120°W to 132°W (Figure 1). The region encompasses an area in which the seasonal coastal upwelling jet closely follows the alongshore topography and mesoscale activity is low (north of ~43.5°N) and an area where the topography is complex and mesoscale activity is high (south of ~43.5°N) [*Strub and James*, 2000]. The highest mesoscale activity in the California Current is reported to occur within our study area offshore and to the south of Cape Mendocino [*Strub and James*, 2000]. The study area also includes the GLOBEC NEP field-study region (42°N–45°N) which surrounds Cape Blanco. We confine most of our analyses to within 3° offshore of the coast and focus on spring through fall, as that is the area and time most relevant to variability in primary and secondary production in the California Current System.

3. Data

[10] We analyze the delayed time, "updated," v1rev4, gridded sea surface height (SSH) anomaly fields produced by Ssalto/Duacs and distributed by AVISO (Archiving, Validation and Interpretation of Satellite Oceanographic, http://www.aviso.oceanobs.com/). Tides have been removed and standard environmental corrections (e.g., inverted barometer, troposphere, ionosphere and electromagnetic bias) applied. The geoid was removed by removing a long-term temporal mean from each grid point. We use the weekly SSH anomaly fields that are gridded to a 0.25° × 0.25° Mercator grid. The interpolation technique is described by *Le Traon et al.* [2003]. Each time-point incorporates six weeks of observations weighted to the central date and merged over multiple satellites to reduce spatial error. In the "updated" version, the gridded products incorporate altimeter data from TOPEX/POSEIDON (T/P), ERS-1, ERS-2, ENVISAT, Geosat Follow-On (GFO), and Jason-1 altimeters, as available, to improve mesoscale mapping resolution [*Pascual et al.*, 2006]. Seasonal cycles are not removed by AVISO. We calculate them by fitting the time series to annual and semiannual harmonics and remove them only when presenting SSH Hovmöller (time-space) diagrams.

4. Methods

[11] We examined the spatial and temporal variability in mesoscale activity from October 1992 to May 2006 using wavelet analyses of the SSH anomaly fields described

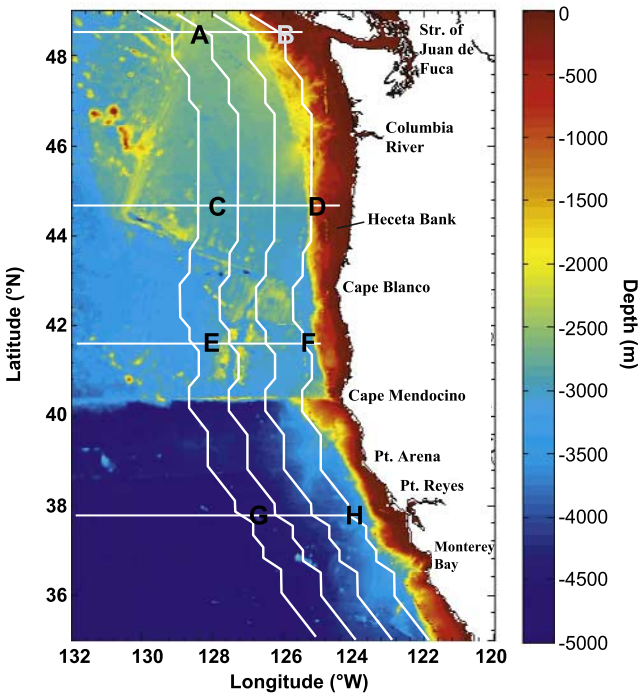

Figure 1. Study area showing bathymetry. Locations where data were extracted for analyses are shown as letters A–H, as alongshore lines at 1°, 2°, 3°, and 4° offshore and as the zonal transects.

above. Satellite altimetry data has been used extensively to study mesoscale circulation in a variety of studies [e.g., *Crawford et al.*, 2000; *Holland and Mitchum*, 2001; *Strub and James*, 2000; *Wilkin et al.*, 2002]. Wavelet analyses provide a method of statistically evaluating temporal changes in energy within specific scales of variability in a time series. The time-averaged wavelet power spectrum is equivalent to the Fourier spectrum, but for analyzing nonstationary signals such as eddies, wavelet analyses have substantial advantages over Fourier analyses in that wavelets retain localized temporal information. This is particularly advantageous for geophysical time series, such as the sea level anomalies analyzed here, that have time-varying frequencies and amplitudes such as those due to local and distant winds, SST, and long-period climate forcings. When the wavelet power is calculated and averaged over a particular band of periods (as in "scale averaging," discussed below), results are similar to an amplified (e.g., squared) band-pass filter.

[12] The wavelet transform (W) is constructed by convolving a time series (x_n) with a scaled (i.e., stretched or compressed) and translated (i.e., moved along the time axis) wavelet (ψ), to produce a 2-D matrix of N data points by s scale factors,

$$W_{j,k} = \frac{1}{\sqrt{s_j}} \sum_{n=0}^{N-1} x_{(n\Delta t)} \psi^* \left(\frac{n\Delta t - b_k}{s_j} \right) \Delta t, \qquad (1)$$

where N is the number of observations in the original time series and Δt is the sampling interval. The scales

$$s_j = j\Delta t,\ j = 2, \ldots,\ J_{\max} \qquad (2)$$

may run from the Nyquist ($2\Delta t$) to $J_{\max}\ \Delta t$, the largest scale of interest which must be <N/2. The translations (time shifts) are

$$b_k = k\Delta t, k = 0, \ldots, N-1, \qquad (3)$$

such that the transform is calculated with its center at each time location in the data series. The factor $1/\sqrt{s_j}$ normalizes the wavelet such that it has constant energy over all scales. The wavelet power is defined as the square of the absolute value of the amplitude of the convolution,

$$\left| W_{j,k} \right|^2. \qquad (4)$$

[13] The wavelet transform acts as a band-pass filter [*Percival and Walden*, 2000] with a width proportional to the scale (s_j): the power spectrum can be thought of as a depiction of how the amplitude of features with a particular periodicity changes with time. The greater the similarity between the signal ($x_{j,k}$) and the wavelet function ($\psi_{j,k}$), the greater the amplitude of the transform. It is important to note that the wavelet power does not measure the absolute amplitude of signals, only the variance within the time window of the scaled wavelet. We give more description of the interpretation of wavelet analyses when discussing the results. We refer the reader to *Meyers et al.* [1993] for wavelet methods comparisons, to *Torrence and Compo* [1998] for the methods used here, and to *Percival and Walden* [2000] for a comprehensive review and mathematical derivation of wavelet analyses for time series applications.

[14] The choice of a wavelet should largely be driven by the shape of the features of interest; preferably, the chosen wavelet is similar in shape to the phenomenon being analyzed. There are many wavelet functions to choose from in the literature, or wavelets can be designed for individual applications. Some wavelets (such as the simple Haar wavelet) are good for identifying sharp edges in a time series. Others, such as the "Mexican Hat" wavelet, are useful for finding individual dips or peaks. *Farge* [1992] describes several of the most common wavelets used in time series analyses. We chose the Morlet wavelet (with frequency parameter = 6) because its shape (a sine wave modified by a Gaussian, dampened to zero on either side of the central time) amplifies smoothly oscillating signals such as the sea level anomalies caused by circulation features. The multiple oscillations in the wavelet's shape integrate over many details of sea level variability that would otherwise complicate interpretation of our results. The Morlet wavelet has additional desirable properties in that it provides a balance between resolution in time and frequency and it is one of the most widely used wavelets in geophysical data analyses.

[15] To evaluate the influence of choosing a particular wavelet function, we also evaluated two other common wavelets: the "Mexican Hat" and "Paul" wavelets [*Farge*, 1992; *Torrence and Compo*, 1998]. All three are nonorthogonal; the Morlet and Paul wavelets are also complex

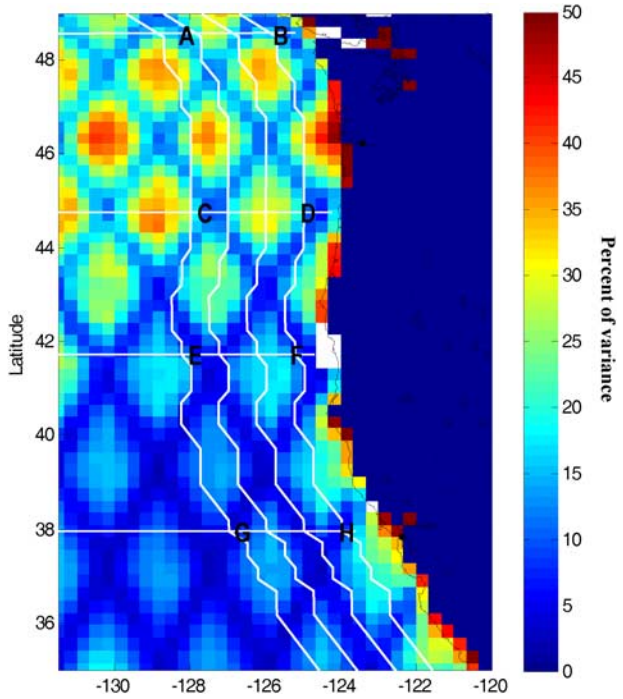

Figure 2. Average error in sea level anomaly due to mapping, expressed as percent of total sea level variance. Estimates at each location were calculated by temporally averaging the error estimates provided by AVISO over the full study period of October 1993 to May 2006. Analysis locations are shown as in Figure 1.

whereas the Mexican Hat wavelet is real-valued, and hence does not preserve phase information. Analyses with the different wavelets all gave similar results though with different temporal and frequency resolution of signals. Owing to its shape, the Mexican Hat wavelet returns sharp peaks in power from individual deviations in sea level, such as those produced by a propagating eddy. Hence, we used the Mexican Hat wavelet to locate the timing of significant peaks in energy more precisely than the Morlet wavelet allows. We also used the Mexican Hat wavelet to determine whether peaks in variance are due to high or low sea level features, which we determined from the sign of the wavelet amplitude before squaring. We used those results in combination with an examination of SSH maps and sea surface temperature (SST) images from the Advanced Very High Resolution Radiometer (AVHRR) or Geostationary (GOES) satellites to identify specific circulation features that resulted in high wavelet power. We describe a few of those features herein, but do not show the individual SSH and SST fields.

[16] For each location A–H shown in Figure 1, we present full wavelet power spectra that are normalized by the variance of each time series. Such spectra provide a measure of the power in each time series with respect to white noise. However, because the variances among time series are not identical (ranging from 13 to 74 cm^2) normalized power in one spectrum is not directly comparable to the normalized power from another time series. Since time series of sea level typically have red spectra (decreasing power over increasing frequency), we calculate 95% significance levels by comparing each wavelet power spectrum to a red noise background spectrum, modeled as univariate lag-1 autoregressive (AR-1) processes generated with variance equal to that of each time series [*Torrence and Compo*, 1998]. Hence, significant power in one spectrum may be lower than nonsignificant power in another. The seasonal cycle is not removed from time series prior to wavelet analyses.

[17] We refer to "mesoscale energy" as the power in mesoscale periods, which we define as 4–18 weeks on the basis of our observations of the development and propagation of features in our study area and previous study of dominant periodicities in the CCS [e.g., *Kelly et al.*, 1998; *Strub and James*, 2000]. To isolate variability in the mesoscale periods from the full wavelet power spectra, we calculate time series of the power averaged over only those periods. We use the methods of *Torrence and Compo* [1998] to calculate these "scale averages." Furthermore, we show results from both 4- to 12-week (hereafter "high-frequency mesoscale energy," or HFME) and 12- to 18-week (hereafter "low-frequency mesoscale energy," or LFME) period bands to distinguish relatively short from relatively longer duration signals. Unlike results showing the full power spectra, the power in these "mesoscale energy" time series is not normalized by the variance, so the energy can be compared among times and locations. However, the 95% significance levels are derived as for the full spectra, so significant power in one time series may be lower than nonsignificant power in another.

[18] Because we calculate wavelet energy at fixed point locations, the periodicity of a signal is determined by the local relationship between a feature's size and propagation velocity. Stationary features such as topographically fixed upwelling filaments or eddies which persist for 4–18 weeks will be resolved in our mesoscale analyses. However, the smallest and largest propagating features may not exhibit energy in the mesoscale periods, depending on their velocities. For example, a small, 50-km-diameter eddy must propagate between 0.4 and 1.75 km/d to be considered mesoscale, whereas a very large (300 km) eddy must propagate at >2.4 km/d. *Kelly et al.* [1998] found that the dominant eddies in the region 33°N–40°N (the southern portion of our study area) had diameters of 100–200 km and westward velocities of ~2.5 cm/s, corresponding to periods of approximately 5–12 weeks.

[19] To simplify discussion, we will refer to scale-averaged wavelet power as "low" if it is <3 standard deviations above the mean power in the full data set (where $\mu = 2.2$ cm^2 and $1\sigma = 2.6$ cm^2); "moderate" if the power is $3–5\sigma$ above the mean; "moderately high" if $5–7\sigma$ above the mean; "high" if $7–8\sigma$ above the mean; and "very high" if $>8\sigma$ above the mean. Those levels correspond to power of approximately 0–10, 10–15, 15–20, 20–25, and >25 cm^2, respectively.

[20] With each weekly gridded sea level anomaly product, AVISO provides an assessment of the errors introduced into the estimates that result from interpolating the data to the full spatial and temporal domain. The error is expressed as the percent of the signal variance at each location. We used a temporal average of these errors (Figure 2) to select specific locations for analyses, balancing low error with geographic spacing that permits regional comparisons. On

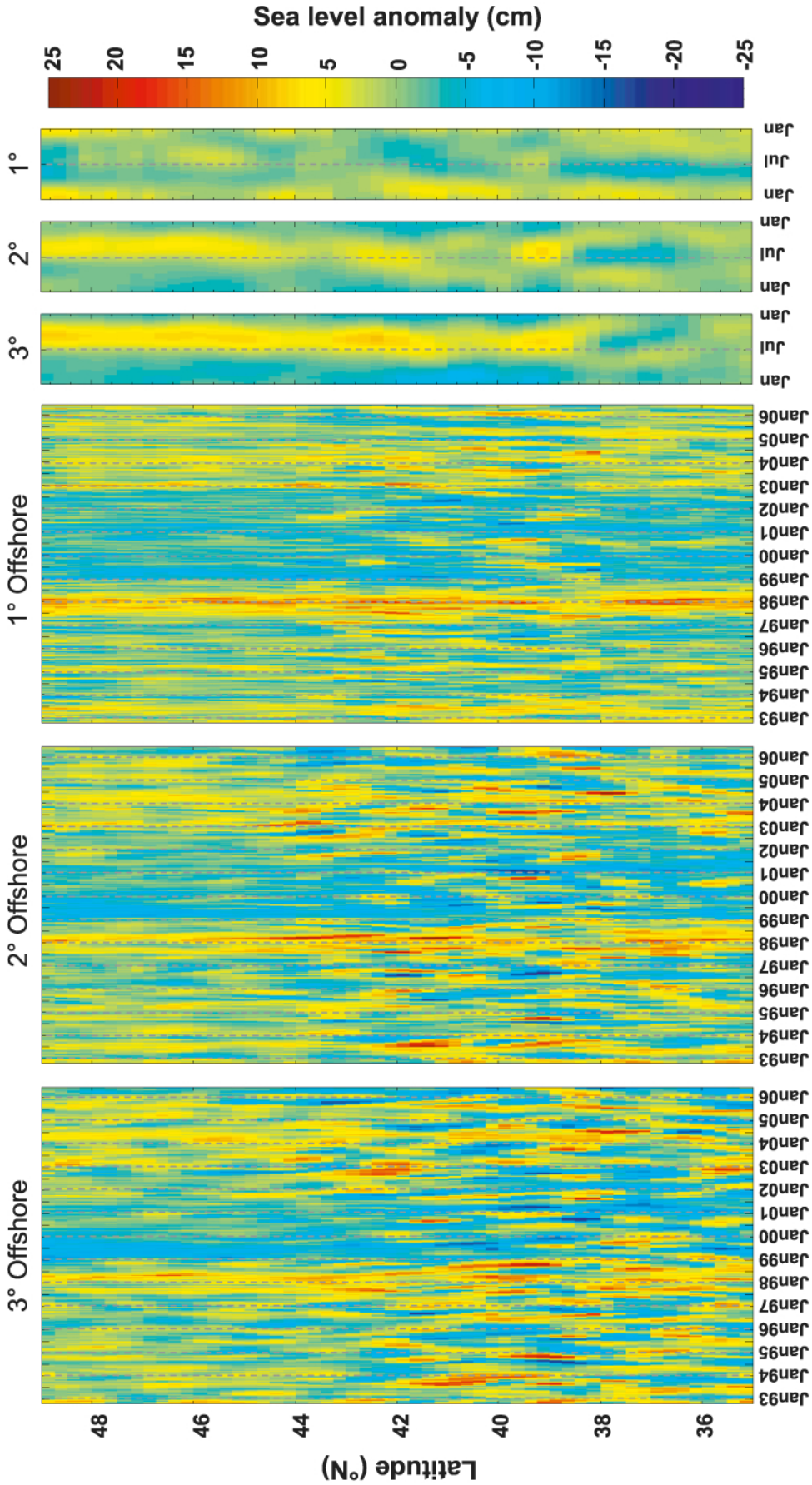

Figure 3. Time-latitude Hovmöller plots of sea surface height anomaly, with seasonal cycles removed, along lines at (left to right) 3°, 2°, and 1° offshore as shown in Figure 1, and (three small right plots) the seasonal (annual + semiannual) cycle along each line.

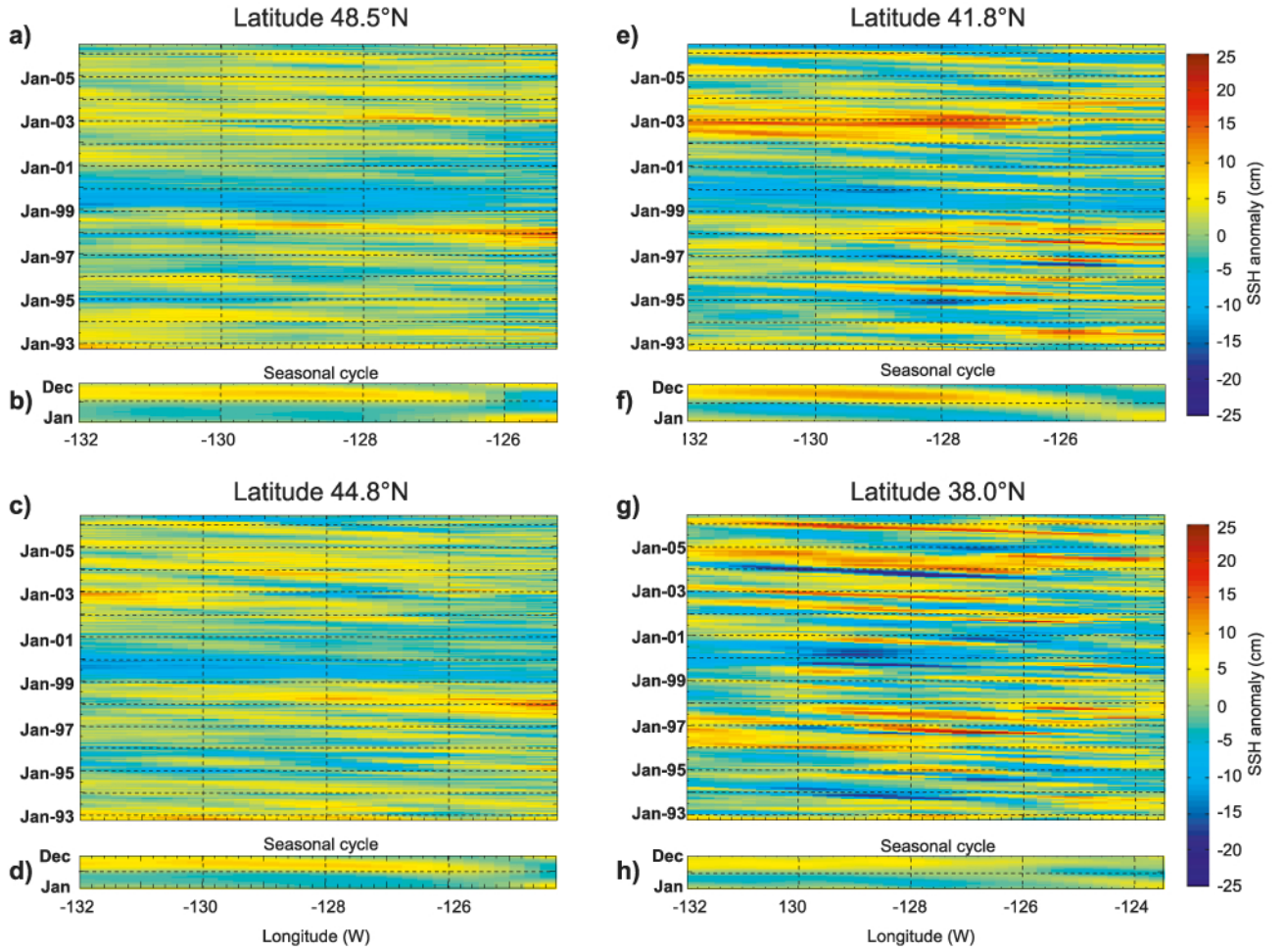

Figure 4. Time-longitude Hovmöller plots of (a) sea level anomaly, with seasonal (annual + semiannual) cycle removed, along latitude 48.5°N, (b) the removed seasonal cycle, (c, d) as above but along 44.8°N, (e, f) along 41.8°N, (g, h) along 38.0°N.

average, lowest error occurs along ground tracks of the T/P and Jason altimeters because of their relatively short orbit periods (9.9 days). Highest errors occur between these tracks in regions with low signal variances. Temporally, mapping error was consistently lowest (<10% of total variance) along those ground tracks, was very high from January 1994 to March 1995 off those ground tracks (>50% error) when only the T/P altimeter was operational, and was low (<20% and mostly <10%) throughout the study area from September 2002 to September 2005 when four altimeters were operational.

5. Results

5.1. Sea Surface Height Anomalies

[21] We show Hovmöller (time-space) diagrams of SSH anomalies along several alongshore and zonal transects to illustrate patterns of variability in contrasting regions of our study area (Figures 3 and 4). Seasonal cycles are a dominant component of variability throughout the study area, although the amplitude and phase varies north to south and onshore to offshore. In the deep ocean (e.g., 2° and 3° offshore, Figure 3), seasonality is exhibited in the regular steric effects of seasonal heating and cooling, with warming leading to maxima in SSH anomalies in fall (~September–November) and cooling leading to minima in spring. Inshore, sea levels peak in December–February from coastal downwelling driven by poleward winds and flow of the Davidson Current. Upwelling causes negative anomalies nearshore in summer. North of latitude 44°N, the seasonal heating and cooling of the ocean is the primary sea level anomaly signal, exceeded only by El Niño/La Niña events (discussed below). Between ~38°N and 44°N, sea level is more temporally and spatially variable, with stronger gradients over shorter spatial scales, indicating higher mesoscale activity in that region. South of 38°N, SSH anomalies show less mesoscale variability inshore, but variability increases offshore.

[22] Climate signals are apparent in the interannual variability in SSH. Most apparent are the extreme high anomalies inshore during the 1997/98 El Niño and the low sea level anomalies during the 1998–2000 La Niña and subsequent summers of 2001–2002. The 2002/2003 El Niño is manifested as weakly positive anomalies and possibly the positive anomalies evident west of 127°W at midlatitudes (Figure 4). The influence of climate is more difficult to discern in areas of high mesoscale variability, such as along latitude 38.0°N (Figure 4), than in areas dominated by longer-period variability. Mesoscale features

develop inshore and propagate westward, disrupting the annual cycle. In Figure 4, such features exhibit an upward inshore to offshore (right-to-left) slope over time as they propagate.

5.2. Wavelet Spectra

[23] Wavelet analyses permit us to extract significant temporal components of SSH anomalies which are difficult to resolve from Figures 3 and 4 alone. We begin our analysis of the SSH variability by showing full wavelet transforms of time series extracted from eight locations (A−H in Figure 1), each location representing a 0.25° × 0.25° grid point of gridded data. We initially focus on two locations as examples of how to interpret the wavelet results. The eight locations were chosen for their low temporally averaged mapping error and their geographic spacing, which facilitates inshore/offshore and north/south comparisons (Figure 2).

[24] In Figures 5 and 6, we present the time series of SSH from each location above its wavelet power spectrum, calculated using the Morlet wavelet. In each spectrum, the y axis is the Fourier period, running from the Nyquist (2 weeks) to <N/2 (here, ∼5 years); the x axis is time. The wavelet power is shown as multiples of the variance in each time series and as such, is a representation of the power with respect to white noise. The amplitude of the power is therefore not comparable among these spectra: a normalized spectrum provides an estimate of the magnitude of the variability relative to the variance at that location. Power above the 95% significance level is contoured in black. The ''cone of influence'' [*Torrence and Compo*, 1998] indicates areas beneath which edge effects may influence results.

[25] To introduce the wavelet results, we compare the locations A and D in Figure 5 (48.5°N, 128.5°W and 44.8°N, 125.0°W). The time series of SSH at Location A shows a clear annual cycle overlaid with shorter-period variability. The resultant wavelet spectrum shows significant energy in the annual (52 week) period throughout the full time series and occasional significant shorter-period variability in periods ranging from ∼2−30 weeks. In contrast, the SSH time series at Location D does not show a clear annual cycle: the variance appears to be contained primarily in short periods. Significant energy with mesoscale periods (4−18 weeks) occurs in most years, with a gap only in 1999−2000. Positive SSH anomalies during the El Niño winters of 1997/1998 and 2002/2003 occur as significant energy with approximately semiannual periods at both locations, especially location D. Finally, note in Figure 5, Location D, that the El Niño/La Niña cycle caused SSH to slowly vary from anomalous highs to lows over 1997−2000. The wavelet transform captures this as significant power with periods of ∼2−3 years, centered on winter 1997/1998. Thus, wavelet spectra extract and amplify the dominant periodic signals in our time series, only some of which are readily apparent to the eye.

[26] With that brief introduction to the interpretation of wavelet spectra, we examine spectra from all eight locations (Figures 5 and 6) to explore general patterns of variability over the domain. There is significant power in a broad range of periods in our study area, with the mesoscale (4−18 week) and annual (52 week) period bands containing a large fraction of the significant power at most locations. Offshore, the annual period dominates the signal in the north where the seasonal steric effect is uninterrupted by mesoscale activity, but loses energy to the south where mesoscale activity is higher. In contrast, inshore, the annual period is not a significant component of the variability except at location B, the shallowest and most northern location (Figure 1), where the seasonal summer upwelling/winter downwelling pattern (e.g., seasonal lows to seasonal highs) causes high energy in the annual band that is out of phase with that offshore. To the south, coastal winds are less seasonal and mesoscale features more frequently cause large deviations in SSH, both processes serving to diminish energy in the annual band.

[27] Moving north to south, energy also shifts away from the very high frequency variability seen in the north into longer-period mesoscale and intermediate-period variability, particularly offshore at Location G (Figure 6). Because the periodicity measured at fixed locations is an interaction between temporal and spatial scales, the shift to longer periods indicates that features have larger length scales and/or slower propagations speeds to the south and offshore. Globally, eddies tend to propagate with characteristic Rossby dynamics [*Chelton et al.*, 2007], so a trend to slower propagation with decreasing latitude is unlikely. A tendency toward increasing spatial scales has been noted by *Ikeda and Emery* [1984] and *Marchesiello et al.* [2003] as filaments extend offshore and as eddies interact and merge as they move to the west. The change in periodicity noted here may reflect those dynamics. Short-period variability at the northern inshore locations (Figure 5, locations B and D) is likely due to coastal upwelling/downwelling dynamics and smaller-scale eddies that are generated over the shelf and slope.

5.3. Mesoscale Power Time Series

[28] In time series of wavelet power that has been scale-averaged over 4- to 12- and 12- to 18-week periods at the eight locations (Figure 7), marked spatial and temporal variability in mesoscale energy emerges. The power in these time series is not normalized, so amplitudes may be compared among locations. Here, we note that the scale-averaged wavelet power is similar to results obtained using amplified (i.e., squared) and smoothed band-pass filtered data.

[29] Offshore, the trend of increasing mesoscale energy with decreasing latitude is consistent with a progression from a more annually dominated region north of Cape Blanco, to a more mesoscale-dominated region to the south. Interannual variability in mesoscale energy is high in the south, particularly at Location G, with energy episodically reaching >7σ above average there. Circulation patterns are particularly complex offshore along this latitude. We found that strong signals from filaments and meanders of the upwelling jet, and strong cyclonic and anticyclonic eddies all contribute to significant mesoscale power there.

[30] Inshore, patterns of variability are tightly related to the bathymetry and coastline topography. The northernmost location (B), lies at the mouth of the Strait of Juan de Fuca where mesoscale dynamics are driven by the topographically fixed Juan de Fuca eddy (centered at ∼48.4°N 125.4°W) [*Hickey et al.*, 1991] which recurs in summer/fall, and by strongly positive winter anomalies in (typically) December/January that may be related to winter downwelling

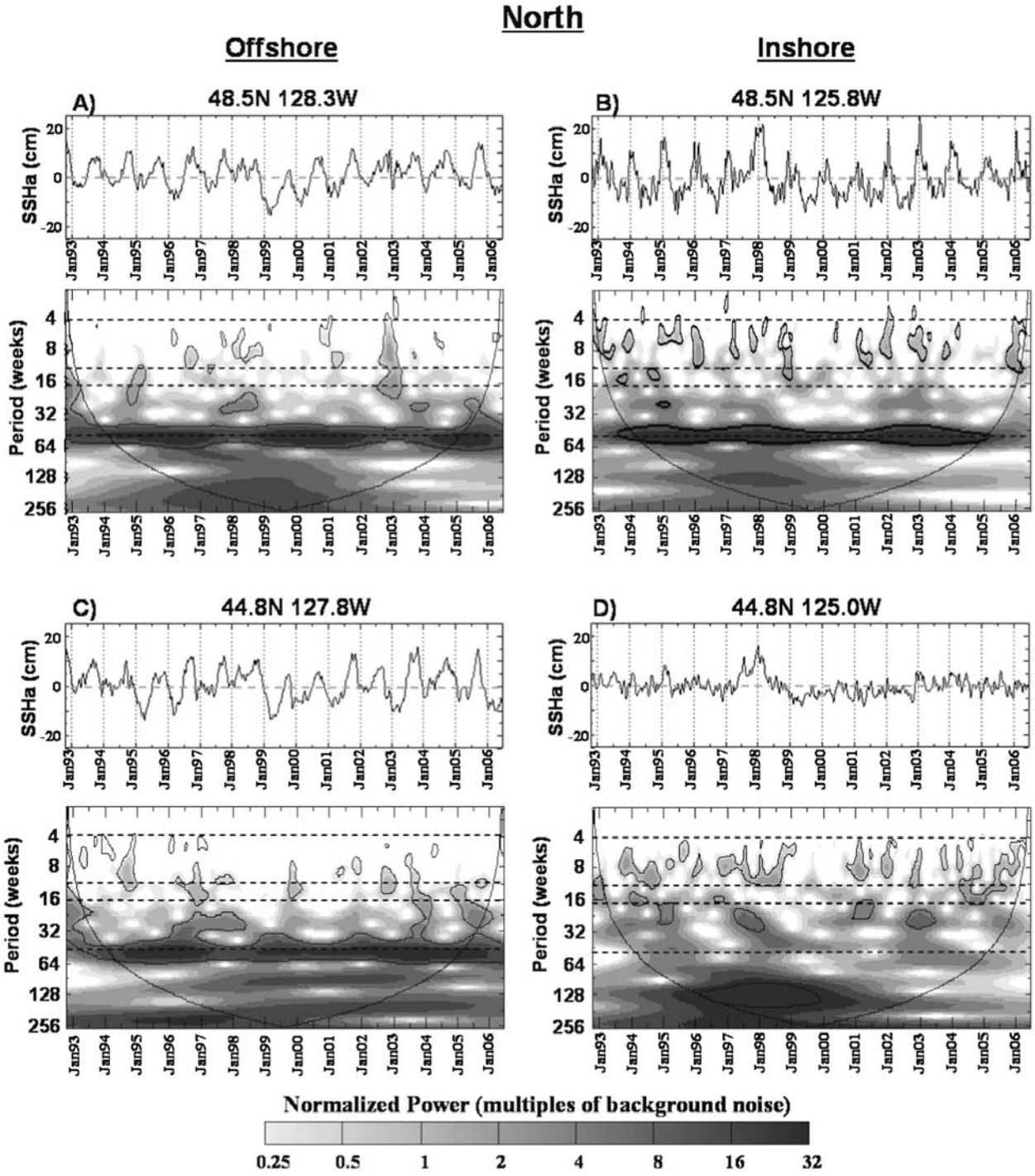

Figure 5. Time series and results of wavelet analyses of sea surface height anomaly at the northern locations: location A, 48.5°N 128.3°W; location B, 48.5°N 125.8°N; location C, 44.8°N 127.8W; and location D, 44.8°N 125.0°W. (top) Individual time series. (bottom) Wavelet power spectra of the time series expressed as multiples of the variance in each time series. Power above the 95% significance level at each location is enclosed in black contours. Below the "cone of influence" are areas where edge effects are important. Horizontal dashed lines are at 4-, 12-, 18-, and 52-week periods.

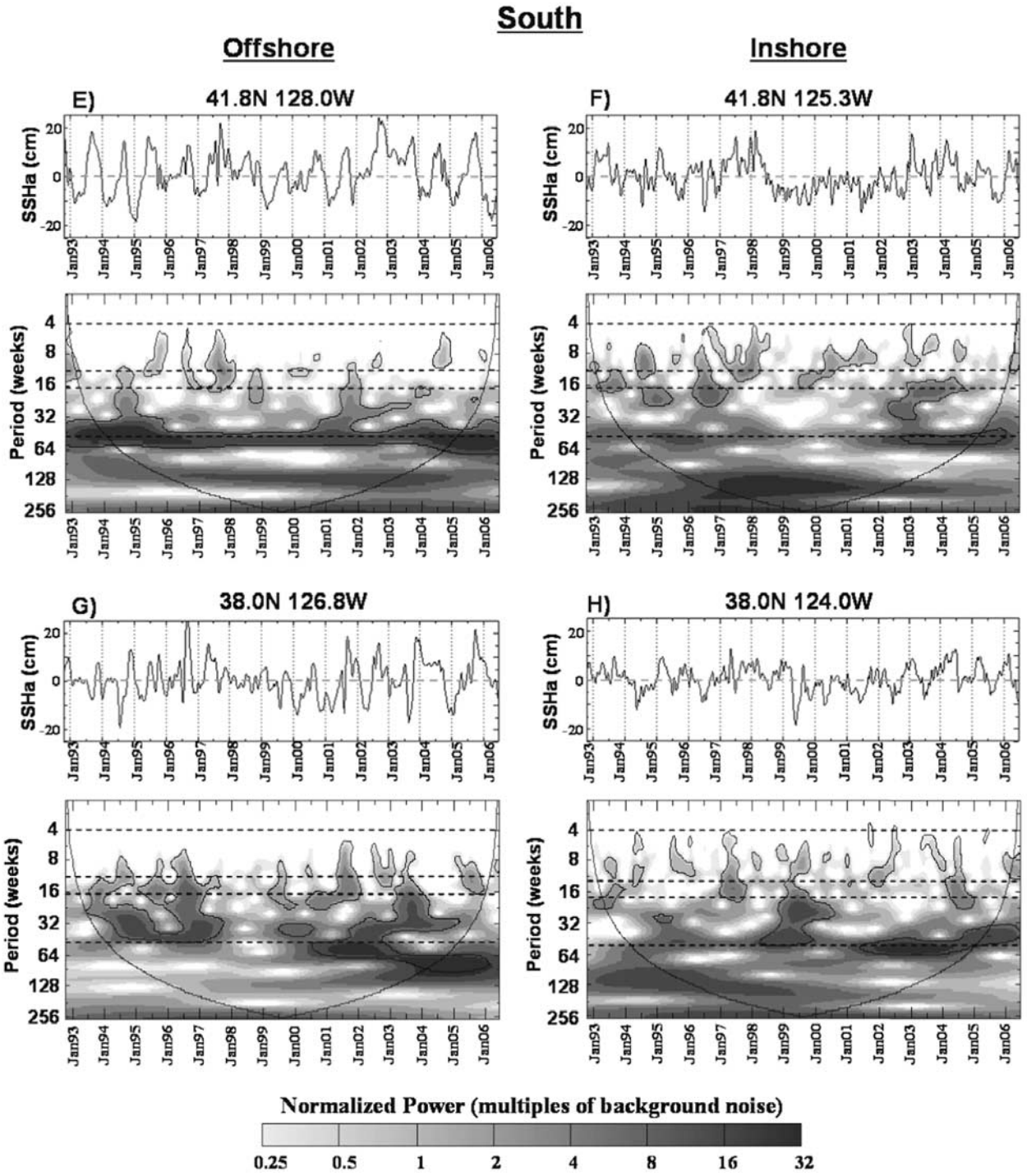

Figure 6. Time series and results of wavelet analyses on sea surface height anomaly at the southern locations: location E, 41.8°N 128.0°W; location F, 41.8°N 125.3°W; location G, 38.0°N 126.8°W; and location H, 38.0°N 124.0°W. All else as in Figure 5.

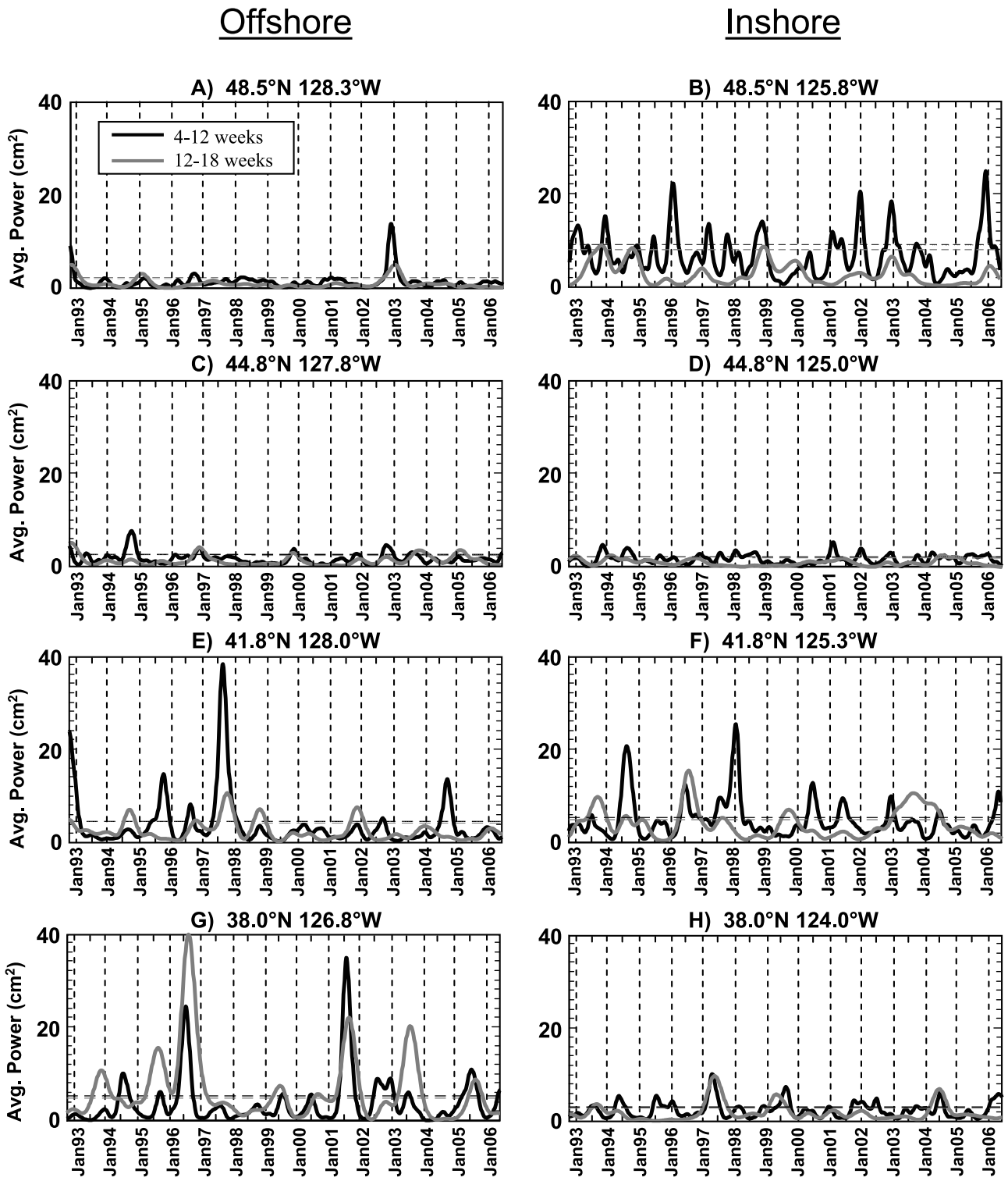

Figure 7. Time series of the scale-averaged wavelet power in the 4- to 12-week period band (black line) and 12- to 18-week period band (gray line) from locations A–H shown in Figures 5 and 6. The corresponding 95% significance levels are shown as horizontal dashed lines.

and freshwater outflow. Farther south, Location D is in the region of a nearly straight north-south coastline where SSH variability (Figure 3) and mesoscale energy is low, rarely exceeding 3σ above the mean. *Legaard and Thomas* [2008] found local minima in intraseasonal variance of SST and chlorophyll in this same region. Moderately high energy occurs in most summers SW of Cape Blanco (Location F), the hypothesized northernmost location at which the summer upwelling jet separates from the coast and becomes an oceanic jet [*Barth et al.*, 2000]. In contrast, SE of Cape Blanco, Location H lies inshore of the meandering upwelling jet following its separation from the coast at Pt. Arena [*Kosro and Huyer*, 1986; *Strub and James*, 2000]. There, energy is low, rarely exceeding 3σ above the mean.

5.4. Spatial and Temporal Variability

[31] A map of temporally averaged energy (Figure 8) gives the visual impression of energy spreading south and to sea, separating from the coastal zone south of Pt. Arena, and peaking almost 400 km offshore. The trend of increasing energy with decreasing latitude, noted at the individual locations above, does not extend to the far south of the domain (Figure 8). Energy in the deep ocean is highest, on average, in a broad area between 36°N and 43°N, 124°W and 130°W, in the vicinity and to the south of the coastal promontories. Overall, patterns of HFME and LFME are similar with a few notable exceptions. Within 1° of the coast, mesoscale energy is dominated by high-frequency variability whereas far offshore, longer-period energy dominates. (Note that the HFME at the mouth of the Strait of Juan de Fuca is anomalous, even compared to other coastal locations.)

[32] In both frequency bands, energy is low along the coast south of Pt. Arena (~39°N). Using RAFOS float observations, *Collins et al.* [2004], also noted a relatively low-energy strip there where floats predominantly moved alongshore. The eastward curvature of the coastline and the separation and seaward movement of the upwelling jet may create this lee south of Cape Mendocino in which energy is low. On the other hand, modeling results predict highest eddy kinetic energy (EKE) nearshore [*Marchesiello et al.*, 2003]. The discrepancy may be due to shorter (<4 week) period variability that is not resolved in this study.

[33] The fan of energy that spreads southwest to sea has its northeast edge near Heceta Bank and Cape Blanco (Figure 8). The role that capes and promontories play in controlling spatial patterns of mesoscale energy in the northern CCS has been well-studied [e.g., *Castelao and Barth*, 2005; *Haidvogel et al.*, 1991; *Lagerloef*, 1992; *Marchesiello et al.*, 2003; *Narimousa and Maxworthy*, 1989; *Strub and James*, 2000]. That variability has been shown to cascade into biological variability [*Henson and Thomas*, 2007a]. North of Heceta Bank (~44.2°N), there are no large promontories so the upwelling jet flows uninterrupted, tightly coupled to the regular alongshore bathymetry [*Barth et al.*, 2005; *Narimousa and Maxworthy*, 1989]. There is some evidence from recent, unpublished studies of nearshore current structure using coastal high-frequency (HF) radar, that the upwelling jet may deviate from the coast around the Columbia River plume (M. Kosro, personal communication, 2007), but appears to turn back to the coast south of the plume without contributing to the generation of energetic offshore mesoscale circulation. We found higher energy in the area between Heceta Bank and Cape Blanco. Peak energy occurs just southwest of Cape Blanco and farther offshore downstream of Cape Mendocino.

[34] LFME shows a strong preference for an offshore area (37°N–38°N, 127°W–128°W) (Figure 8) that our study of SSH and SST images revealed as a location at which northwestward-turning, cold upwelling filaments generated between Pt. Arena and Pt. Reyes frequently interact with strong anticyclonic, SW propagating eddies (an animation of 1 year is provided as an example in auxiliary material[1]). Historically, the cold filament had been noted in satellite SST images in many summers and was sampled during the Coastal Transition Zone (CTZ) Program in the 1980s [*Strub et al.*, 1991]. *Lagerloef* [1992] subsequently described the anticyclonic eddies as annually recurring, topographically controlled features that are dynamically coupled to the filaments. Thus, the time-averaged pattern of energy reflects the strong influence of topography on circulation, even hundreds of km to sea.

[35] Extracting the temporally integrated information along offshore transects (Figure 8) emphasizes the spatial patterns described above and, in combination with annual cycles of energy (Figure 9), indicates a seasonal SW progression of energy from nearshore generation in spring to peak levels offshore in summer/fall. Spatially averaged, mesoscale energy peaks regularly in summer/fall (Figures 9 and 10) as has been previously reported [*Collins et al.*, 2004; *Strub and James*, 2000]. Energy tends to peak 1°–1.5° farther south and 2–3 months later offshore compared to inshore. Energy at 1° offshore peaks in July, energy 2° offshore peaks in July/August, energy 3° offshore peaks in August, and 4° offshore, energy peaks in September/October. Both the SW propagation of many eddies and the separation and westward movement of the coastal upwelling jet after separating from the coast at the capes are likely mechanisms for the apparent progression of energy. *Kelly et al.* [1998] reported a westward movement of EKE between 125°W and 128°W that they ascribed to the seasonal offshore movement of the core of the CC south of 40°N.

[36] *Kelly et al.* [1998], *Strub and James* [2000], *Chereskin et al.* [2000], and *Marchesiello et al.* [2003] all reported an onshore to offshore decrease in EKE in the CCS. We find a general trend of lower energy at sea, particularly high-frequency energy (Figures 8 and 9), but between 2° and 4° offshore, the pattern is time-dependent (Figure 9). In spring and early summer, energy (particularly HFME) increases more quickly inshore than offshore. However, in fall and winter, as nearshore energy declines, energy is peaking offshore, causing higher levels of energy offshore at that time. Also note from Figure 10 that there is a great deal of interannual variability in both the relative timing of peak energy from nearshore to offshore, and the relative amplitude of peaks. That there is not a consistent pattern of lower amplitude peaks in energy occurring later in the year offshore indicates that there are important mechanisms of energy generation or intensification offshore. One

[1] Auxiliary materials are available in the HTML. doi:10.1029/2007JC004256.

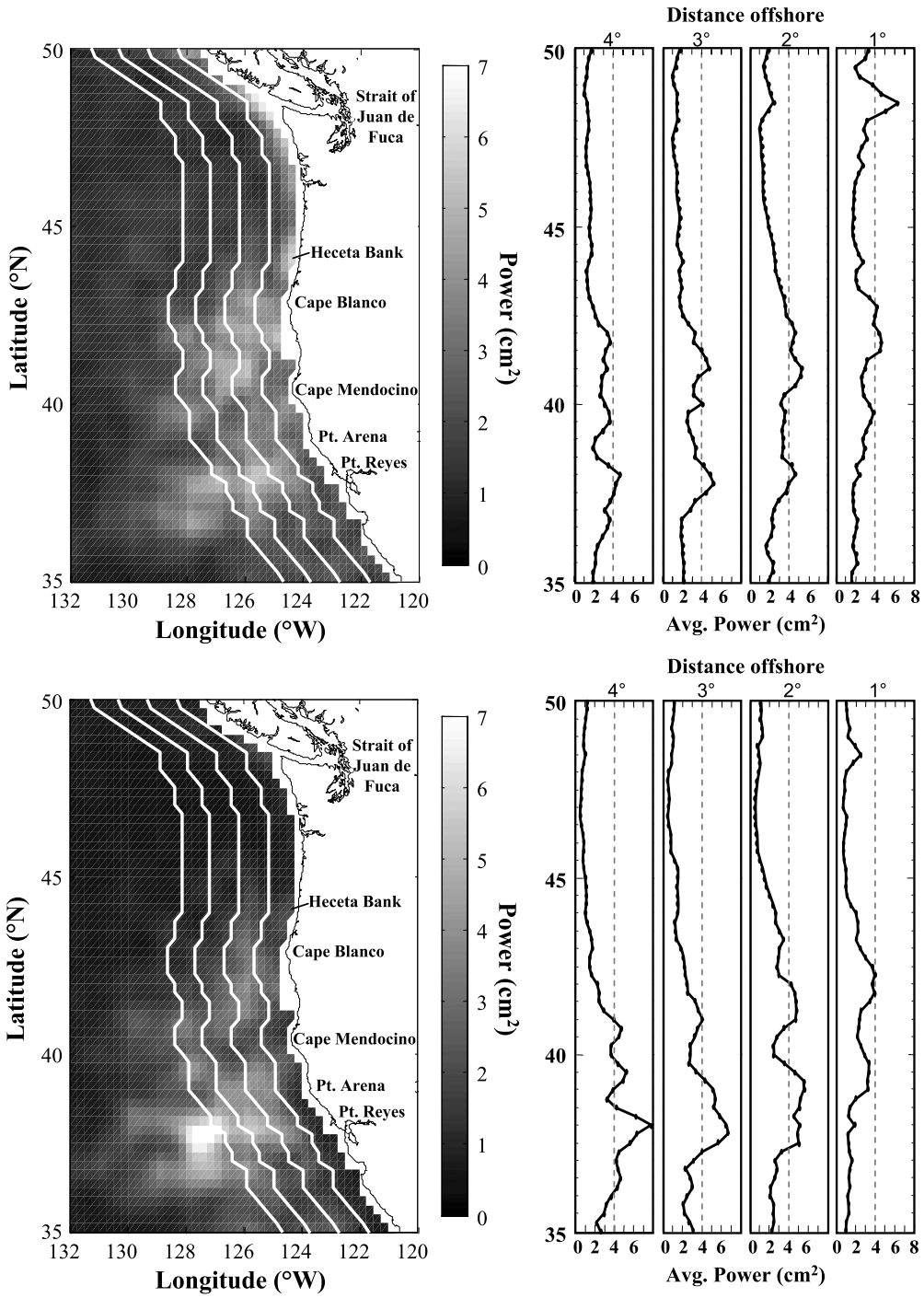

Figure 8. Temporally averaged wavelet power over the study area in the (top) 12- to 18-week and (bottom) 4- to 12-week periods. White lines parallel to the coast indicate the 1°, 2°, 3°, and 4° offshore lines used in analyses. Power along those lines are extracted and shown to the right to clarify spatial patterns of variability.

such mechanism may be the interaction of oceanic expressions of features, as exemplified by the interaction between offshore expressions of eddies and upwelling filaments noted above. Others may be effects of submarine ridges (such as the Mendocino escarpment) [*Narimousa and Maxworthy*, 1989] or areas of intensified flow [*Kelly et al.*, 1998].

[37] We find significant wavelet power beyond 132°W at all latitudes (>800 km offshore of central California, not shown) although energy is strongly dampened that far to sea, and note that the signatures of upwelling filaments, cyclonic, and anticyclonic eddies are visible in sea level anomaly maps at least that far to sea. *Strub and James* [2000] also reported statistically significant EKE calculated from sea surface height gradients as far as 130°W off central

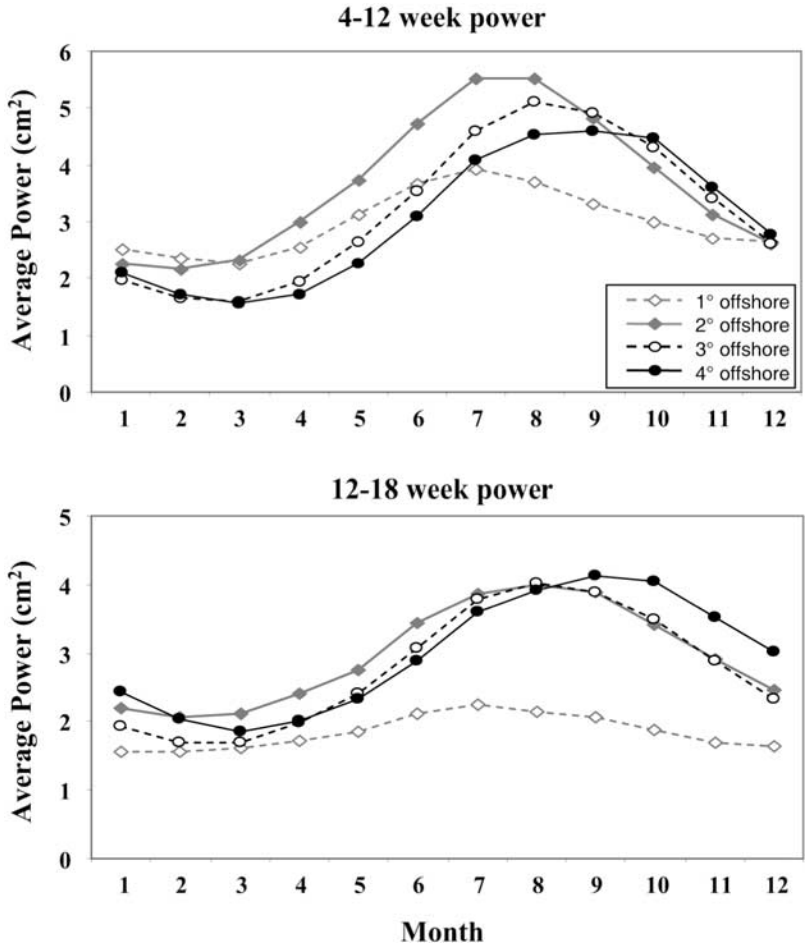

Figure 9. Seasonal variability of mesoscale energy with (top) 4- to 12-week and (bottom) 12- to 18-week periods. Cycles were created by averaging all values in each month, along lines 1°, 2°, 3°, and 4° offshore between 36°N and 43°N.

California (and as far as 135°W off Baja, California) and *Marchesiello et al.* [2003] modeled filaments and eddies that carried coastal water far to sea.

6. Discussion

6.1. Seasonal Variability

[38] Consistent with previous studies [e.g., *Kelly et al.*, 1998; *Marchesiello et al.*, 2003; *Strub and James*, 2000], we found that mesoscale circulation in the northern California Current typically peaks during summer and fall (Figure 9) when winds and alongshore transport are primarily equatorward. As the coastal upwelling jet migrates offshore through the summer [*Strub and James*, 2000], it pinches off eddies, both inshore in anticyclonic bends of meanders, and offshore at the tips of energetic, cyclonically and anticyclonically turning filaments. Those filaments and eddies that propagate westward to the deep ocean can transport large masses of water and coastal organisms to sea [*Chereskin et al.*, 2000; *Cornuelle et al.*, 2000; *Mackas et al.*, 1991]. Like others [e.g., *Kelly et al.*, 1998; *Marchesiello et al.*, 2003], we note a progressive movement of seasonal currents and energy offshore into the deep ocean on an annually recurrent cycle. In winter, winds and currents in the northern CC are poleward and coastal downwelling dominates the inshore region. Consistent with model results which predict that poleward coastal jets generate less EKE than equatorward jets [*Haidvogel et al.*, 1991] we found that mesoscale energy is at a minimum at this time, despite high coastal sea levels and strong winter winds.

6.2. Relationship to Climate

[39] Below, we explore the relationship between climate variability and interannual variability in mesoscale circulation, and consider potential local and basin-scale forcing mechanisms. To examine temporal variability in mesoscale energy integrated over the northern California Current, we define an index of the total mesoscale variability in the region. The index consists of time series of wavelet power in the mesoscale period bands averaged between 1° and 3° offshore, 36°N–43°N (Figure 11, first two plots). We refer to these spatially averaged time series as the total mesoscale energy in the northern California Current. We restrict the index to within 3° of the coast because westward propagation of energy, which results in highest energy occurring offshore later in the year than inshore, causes a smearing of the temporal signal if integrated far to sea. Because instabilities in the coastal upwelling jet and California Undercurrent are believed to be the primary sources of mesoscale circulation in the northern CCS [*Chereskin et al.*, 2000;

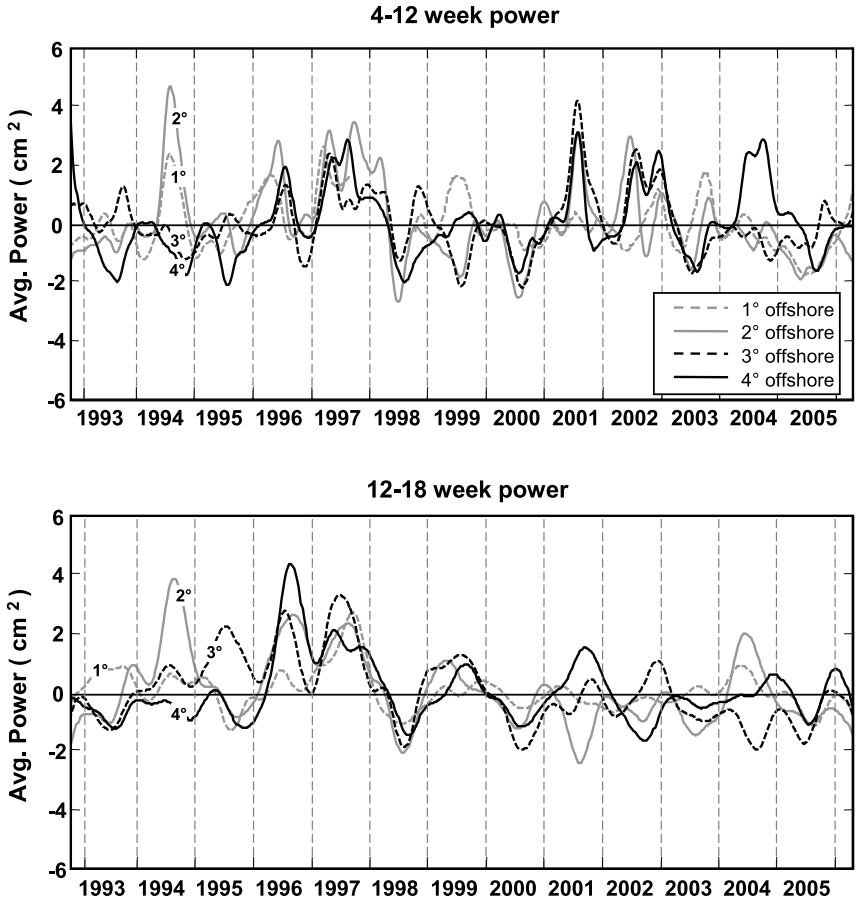

Figure 10. Wavelet power in the (top) 4- to 12-week and (bottom) 12- to 18-week period bands averaged over latitudes 36°N–43°N along lines at 1°, 2°, 3°, and 4° offshore, as shown in Figure 1.

Marchesiello et al., 2003], restricting the index to within 3° of the coast, where the strongest alongshore currents reside, emphasizes temporal patterns in the generation of features and simplifies comparisons to indices of climate and local forcings.

6.2.1. The 1997/1998 El Niño

[40] Visually, the clearest climate signal in our time series of total mesoscale energy is the suppressed energy in the middle of our study period (1998–2001) which coincides with the end of the 1997/1998 El Niño and the subsequent La Niña. On closer inspection, anomalous energy during the 1997/1998 and 2002/2003 El Niño events also stand out as a pattern of elevated energy during the winter followed by suppressed energy in the following spring/summer.

[41] The physical effects of the 1997/1998 El Niño on the CCS are well described in the literature [e.g., *Collins et al.*, 2002; *Huyer et al.*, 2002; *McPhaden*, 1999; *Strub and James*, 2002b]. The first definitive signal of the El Niño arrived off central California in June and off Oregon in July 1997 as elevated temperatures, high coastal sea levels, and anomalously poleward flow [*Collins et al.*, 2002; *Huyer et al.*, 2002; *Kosro*, 2002]. In the northern CC, strongest sea level anomalies occurred in September 1997 through February 1998 with poleward flows off the shelf break exceeding 60 cm/s (>3× higher than average) in November [*Kosro*, 2002]. The high coastal sea levels caused an offshore pressure gradient and resulted in eddies shedding off to sea. Atmospheric teleconnections in the form of anomalously strong winter winds and southwesterly storms (Figure 11, third plot) further served to input energy into the system. Several other studies in the NEP have reported increased eddy generation during El Niño events due to increased winds or flow [e.g., *Melsom et al.*, 2003, 1999; *Zamudio et al.*, 2001].

[42] In 1997, HFME increased in spring as usual, reaching a normalized peak of 0.6 in May/June (Figure 11, first plot). Because the first strong signs of El Niño did not reach central California until June 1997, that peak, although early, was probably a "normal" summer peak in energy. However, the subsequent peak (of 0.8) in September/October 1997 was likely influenced by the El Niño as the amplitude was anomalously high and the timing corresponds with strong poleward transport and anomalous hydrography in the northern CC. Strong poleward advection persisted through February 1998 in the northern parts of the CCS [*Strub and James*, 2002b] (see also Figure 11). Mesoscale energy declined more slowly than usual that winter, resulting in the highest winter HFME in our record, and did not drop to a minimum until June 1998, 3–4 months later than average. In fall 1998, a small increase in energy followed the return to near-normal temperatures, strong upwelling-favorable winds, and equatorward transport throughout the CCS (Figure 11).

[43] The weaker 2002/2003 El Niño had a similar, though moderated, pattern of energy (Figure 11). Energy was anomalously high during winter when poleward winds were anomalously strong (Figure 11, third plot) and stayed high until slightly later than normal before dropping to a minimum in late March (HFME) or April (LFME). The largest difference in energy between the two El Niño events is that energy in summers 2002 and 2003 was not obviously influenced by the El Niño: the elevated energy was confined to winter. In 2002, sea level was not anomalously high until

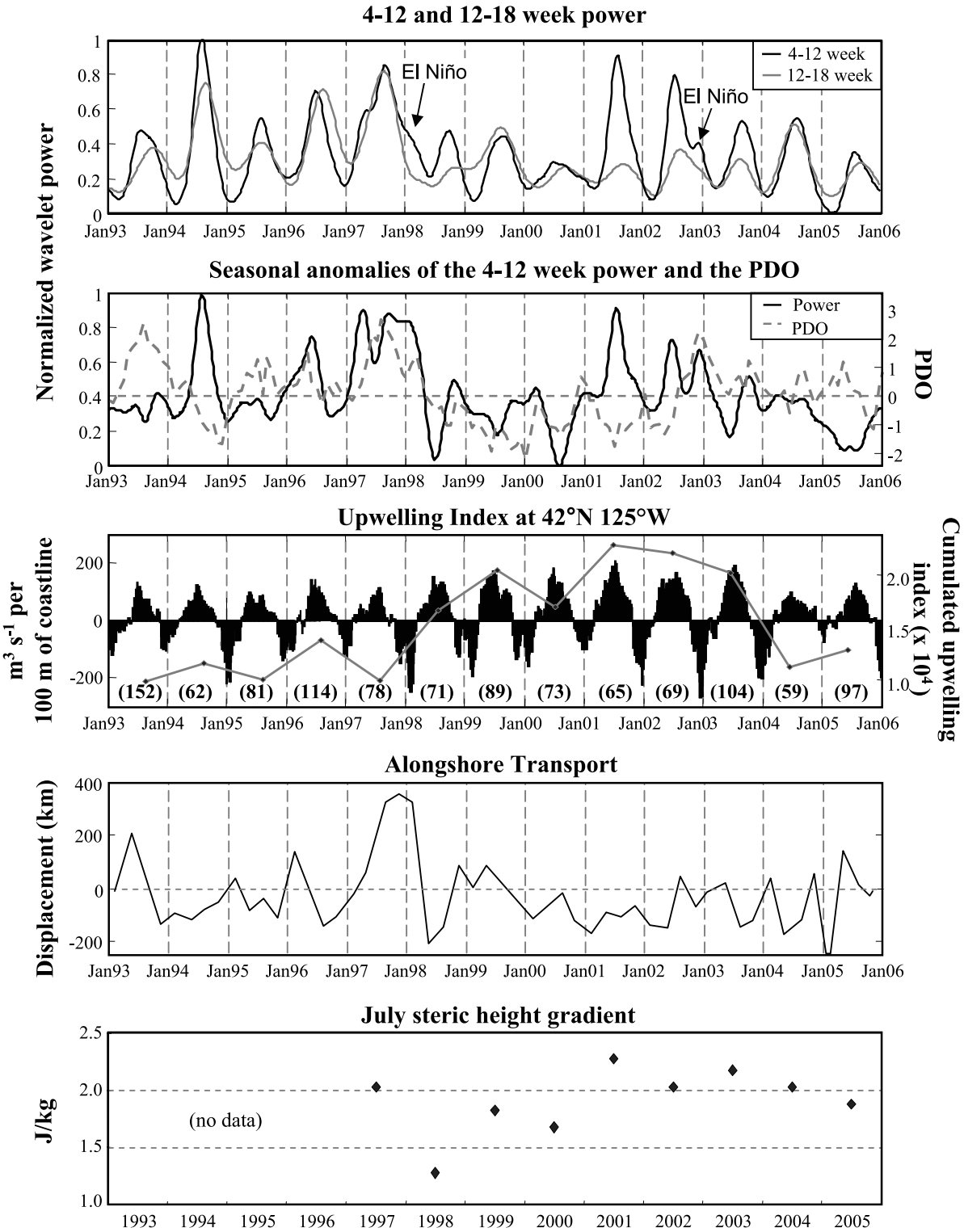

Figure 11

December (Figure 3) and transport was normal (Figure 11), which indicates that the increased winter energy may have primarily been due to atmospheric teleconnections in the form of anomalously strong winds.

6.2.2. Winds and Transport

[44] The generation and evolution of mesoscale circulation are ultimately controlled by the energy in the system. Locally, that energy may derive from winds, currents moving into the area, and density gradients. In a seasonal upwelling system, winds vary in both the timing of the ''spring transition'' (ST) from primarily downwelling-favorable to primarily upwelling-favorable winds and their intensity and duration through the season. Thus, we explore mechanisms of mesoscale variability by comparing the interannual variation in energy to the timing of the ST, the cumulative intensity of upwelling-favorable winds over the summer, the strength (equatorward transport) of the CC, which varies independently of local wind-forcing [*Strub and James*, 2003], and to density gradients.

[45] We used the methods of *Pierce et al.* [2006] to calculate the date of the ST at three latitudes (39°N, 42°N, and 45°N) using the Coastal Upwelling Indices (CUIs) produced and provided by the NOAA-Fisheries laboratory in Pacific Grove, CA (http://www.pfeg.noaa.gov/products/PFEL/modeled/indices). Because winds and currents are highly variable during spring in the CC, it is not simple to determine a precise date of the spring transition, although many have endeavored to do so [e.g., *Kosro et al.*, 2006; *Pierce et al.*, 2006; *Schwing et al.*, 2006] with often similar, but sometimes substantially different, results. The climatological date of the ST in the CC is generally earlier at decreasing latitudes [*Schwing et al.*, 2006]. In any particular year, however, a southern location may have delayed onset of upwelling whereas onset at northern locations may occur anomalously early, reversing the general pattern. Keeping those potential complications in mind, we present the annual Julian date of the ST and the daily CUIs from 42°N 125°W as a representation of the northern CCS wind-forcing (Figure 11, third plot). In 1993–2005, the timing was always $ST_{39N} \leq ST_{42N} \leq ST_{45N}$. The only years in which the transition did not show a consistent decrease in timing with latitude were 1993 ($ST_{39N} \ll ST_{42N} = ST_{45N}$), 2000 ($ST_{39N} < ST_{42N} \ll ST_{45N}$), and 2003 ($ST_{39N} \ll ST_{42N} = ST_{45N}$).

[46] Also as in work by *Pierce et al.* [2006], we calculated an index of the integrated seasonal intensity of upwelling by accumulating the CUIs from the calculated date of the ST through 1 October. Again, we present only those at 42°N 125°W (CU_{42N}) (Figure 11, third plot). Interannual patterns of accumulated upwelling over the season were similar among the three locations despite some differences in the date of the ST.

[47] Nonseasonal anomalies in the transport into the CC (Figure 11, fourth plot) were provided by C. James (Oregon State University). Transport anomalies were estimated geostrophically as in work by *Strub and James* [2003] from the east-west gradient in altimeter sea surface height averaged over the region 45°N–53°N. Geostrophic transport of the CC may affect mesoscale energy by enhancing wind-driven equatorward currents in summer when transport is also equatorward (negative) or by diminishing wind-driven currents when transport anomalies are poleward (positive).

[48] In several years, winds and transport anomalies appear to explain the annual level of mesoscale energy (Figure 11). For instance, total mesoscale energy was low in 1993 and 2005, years of very late STs, weak upwelling, and northward CC transport anomalies. Energy was high in 2001 and 2002, years of early STs, strong upwelling, and anomalously high equatorward transport. However, contrary to our expectations based on winds and transport, energy was at a minimum in 2000 when upwelling was moderate, the ST was slightly early, and alongshore transport was moderately equatorward. Furthermore, energy was at a maximum in 1994, a year of moderately early STs, southward transport, but relatively weak upwelling. (Note that results from 1994 should be interpreted with caution because only one altimeter was operational, so gridding errors were high.) The higher energy in summer 1996 compared to 2003 also counters our hypothesis: STs were late both years, transport was similar in spring/summer of both years, yet weak upwelling in 1996 compared to strong upwelling in 2003 resulted in opposite energy levels than predicted. Though *Pierce et al.* [2006] found a significant correlation between annually accumulated upwelling indices and anomalies in available potential energy along 44.7°N, we do not find that upwelling translated directly to mesoscale energy in any obvious way. Overall, upwelling and transport indices did not consistently relate to the annual amplitude of mesoscale energy; controls on mesoscale energy are more complex than those few indices can explain.

6.2.3. Pacific Decadal Oscillation, Climate, and Available Potential Energy

[49] Because energy did not correspond closely to local forcings, we investigated the relationship between mesoscale energy and basin-scale indices of climate relevant to the NEP (e.g., the PDO, MEI, and NOI) for evidence of an influence by remote forcing. The MEI is positively related to high energy during fall/winter 1997 and winter 2002/

Figure 11. (first plot) Normalized wavelet power in the 4- to 12- and 12- to 18-week mesoscale periods averaged over the area from 1° to 3° offshore between 36°N and 43°N, the area of highest mesoscale energy. (second plot) The normalized 4- to 12-week period power overlaid on the PDO, seasonal cycles removed from both. (third plot) The Coastal Upwelling Index at 42°N 125°W from NOAA PFEL (bars), the index accumulated annually from the date of the spring transition through 1 October (points), and the annual Julian day of the spring transition (in parentheses). (fourth plot) Three-month averaged, nonseasonal anomalies of alongshore transport into the northern California Current calculated from sea level gradients between 45°N and 53°N within 250 km of the coast as in *Strub and James* [2003]. Positive anomalies indicate poleward transport. (fifth plot) Gradient in steric height (in J/km) between stations 9 and 80 km offshore at 44.7°N during July cruises. A gradient of 1 J/kg is equivalent to a 10-cm change in layer thickness.

2003, but otherwise does not predict energy levels well. HFME corresponded more strongly to the PDO than to the indices of wind and transport (Figure 11, second plot) or the NOI (not shown). Energy was low in most years of negative PDO despite relatively strong winds, and moderate to high in most years of a positive PDO. Notable exceptions are 2001, an unusual year in which HFME was strongly decoupled from LFME indicating that different processes may have been important in the generation of mesoscale energy compared to other years, and 1994 (again with the caution that only one satellite was operational). HFME lagged the PDO by 3 months and was correlated with r = 0.31 (p-critical = 0.30 with N* = 44).

[50] The weakly significant correlation between the PDO and HFME indicates that basin-scale processes may affect mesoscale circulation. Weak density gradients and low available potential energy (APE) have been hypothesized to cause low mesoscale activity during El Niño events at low latitudes [*Durazo and Baumgartner*, 2002; *Hormazabal et al.*, 2004]. Though we report an increase in energy during the peak of the El Niño due to intensified poleward winds and currents, mesoscale energy was strongly damped the following summer of 1998. That summer, ocean temperatures remained elevated at depth and hence cross-shelf density gradients were weaker than usual despite strong upwelling-favorable winds [*Huyer et al.*, 2002].

[51] Therefore, we explored the hypothesis that the relationship between mesoscale energy and climate is through the system's APE. The APE can be determined by horizontal density gradients which in coastal upwelling systems are strongly affected by two factors: upwelling-favorable winds, and vertical density gradients. Winds provide the kinetic energy to upwell water from depth, generating upward-sloping isopycnals; the vertical density gradient determines the resultant horizontal gradient. The PDO is derived from the first principal component of North Pacific basin-scale SST [*Mantua et al.*, 1997], hence CCS surface temperatures are strongly correlated with the PDO. The sea surface along the U.S. West Coast is anomalously cool during a negative PDO and anomalously warm during a positive PDO. But because the sign of the PDO does not connote a change in temperatures at depth, and temperatures at depth are lower than near-surface, stronger vertical upper-ocean temperature gradients may occur during some years of a positive PDO than during a negative PDO. Hence, largest cross-shelf gradients could occur in years of both a positive PDO (when surface temperatures are anomalously high) and strong upwelling-favorable winds and vice versa. Evidence that long-term patterns in stratification are related to the PDO is given by *Bograd and Lynn* [2003] who reported that stratification in the California Bight increased following the 1976 "regime shift," a climate shift which corresponded to a change from a mostly negative to a mostly positive PDO. We would not expect the trend to hold for each year of the time series, but Bograd and Lynn's study provides a hint that variability in basin-scale stratification may be effecting circulation energy.

[52] Although few long-term hydrographic studies have been conducted in our study area with which to test the link between mesoscale energy and APE, we examined hydrographic data collected by A. Huyer (Oregon State University) along a transect at 44.7°N each July of 1997–2005 as part of the GLOBEC NEP program. Horizontal gradients in steric height provide an estimate of gradients in the density of the underlying water column, thus, for each cruise we estimated the APE in the upwelling system as the gradient in steric height (geopotential anomaly) across the frontal upwelling jet between stations 9 km (Station "NH5") and 80 km ("NH45") from shore [from *Huyer et al.*, 2007] (Figure 11, fifth plot).

[53] We found that the cross-shelf steric height gradient measured in July 1998 was the lowest in the 9-year record, and hence may help explain the low HFME that summer. Over all years, we found Pearson's r = 0.60 (p = 0.09) between the annual maximum in HFME and the July APE. When we either correlate the July APE with HMFE on 1 August (instead of the maximum amplitude, which varied in timing annually) or remove 1998 from the relation (the year of greatest temporal separation between the timing of maximum energy and the July occupation of the hydrographic transect), the correlation increases to r = 0.70 or r = 0.82 and the relationship is significant (p = 0.05 or 0.02) even when using a reduced N* = 7 to account for the low serial correlation in APE among years.

[54] Our confidence in the link between APE and mesoscale energy is tempered by the few (nine) years in which we have measurements of APE and that the APE on a single occupation of a transect is in part influenced by recent wind conditions and not entirely by conditions integrated over the prior months. However, the significant correlation between APE and HFME indicates that a link exists between the two, thus demonstrating a relationship between basin-scale processes and regional mesoscale energy in the CCS. Modeling efforts and the increasing availability of in situ information may help resolve the relationship in the future.

7. Conclusions

[55] The dynamics of cross-shelf transport of biological production have been a recurrent theme of study in upwelling systems. Large volumes of coastal water can be advected offshore in mesoscale circulation features [*Kosro et al.*, 1991], so variability in the generation and energy in such features can have profound implications for biological processes. The transport by mesoscale features can effect populations of organisms in many ways: by redistributing coastal species into the deep ocean and oceanic species onto the shelf [*Mackas and Coyle*, 2005], redistributing nutrients available for production, preventing retention of species in critical nearshore habitat, creating offshore areas of localized production [*Legaard and Thomas*, 2006], and creating local "hot spots" of upper trophic activity [*Palacios et al.*, 2006].

[56] Mesoscale geostrophic features with spatial scales of >50 km are dominant circulation features in the CCS [*Brink et al.*, 2000; *Powell et al.*, 2006], contributing ~80% of the total variance in sea level [*Marchesiello et al.*, 2003]. Herein, we have presented a statistical analysis of the variability in mesoscale energy in the northern CCS that allows us to separate years and areas of high and low energy. Our results suggest that mesoscale circulation energy in the northern CCS is moderated by climate. We hypothesize that energy is proximally controlled by the APE in the

system and that the APE is ultimately controlled by both local and basin-scale processes. Vertical density gradients (surface to ~150 m depth) may be controlled by basin-scale processes; gradients may be converted to tilted isopycnals and horizontal gradients by local upwelling winds. Our index of mesoscale variability will be useful to compare to other physical and biological parameters as a step toward understanding the mechanisms of variability in marine ecosystems.

[57] **Acknowledgments.** The altimeter products were produced by SSALTO/DUACS and distributed by AVISO with support from CNES. Wavelet software was provided by C. Torrence and G. Compo, and is available at http://paos.colorado.edu/research/wavelets/. We thank C. James for providing ancillary data, M. Saraceno for helpful discussions, and T. Cowles, W. Peterson, and two anonymous reviewers for comments which improved the manuscript. Support for J.E.K. was provided through Oregon State University's Cooperative Institute for Marine Resources Studies, award NA17RJ1362 from the National Oceanic and Atmospheric Administration (NOAA), U.S. Department of Commerce (DOC) and through the U.S. GLOBEC Northeast Pacific Program on NSF grant OCE-0435619. Support for P.T.S. was provided by NOAA/NESDIS through the Cooperative Institute for Oceanographic Satellite Studies (NOAA grant NA03NES4400001), the U.S. GLOBEC project (NSF grant OCE-0000900) and NASA/JPL (grant JPL-1206714 - OSTM). The statements, findings, conclusions, and recommendations are those of the authors and do not necessarily reflect the views of NOAA or the DOC. This paper is contribution 567 from the U.S. GLOBEC program, jointly funded by the National Science Foundation and NOAA.

References

Bakun, A. (1990), Global climate change and intensification of coastal ocean upwelling, *Science*, *247*, 198–201.

Barber, R. T., and R. L. Smith (1981), Coastal upwelling ecosystems, in *Analysis of Marine Ecosystems*, edited by A. R. Longhurst, pp. 31–68, Academic Press, San Diego, Calif.

Barth, J. A., S. D. Pierce, and R. L. Smith (2000), A separating coastal upwelling jet at Cape Blanco, Oregon and its connection to the California Current System, *Deep Sea Res., Part II*, *47*, 783–810.

Barth, J. A., S. D. Pierce, and T. J. Cowles (2005), Mesoscale structure and its seasonal evolution in the northern California Current System, *Deep Sea Res., Part II*, *52*, 5–28.

Batteen, M. L. (1997), Wind-forced modeling studies of currents, meanders, and eddies in the California Current system, *J. Geophys. Res.*, *102*(C1), 985–1010.

Bograd, S. J., and R. J. Lynn (2003), Long-term variability in the Southern California Current System, *Deep Sea Res., Part II*, *50*, 2355–2370.

Brink, K. H., R. C. Beardsley, J. Paduan, R. Limeburner, M. Caruso, and J. G. Sires (2000), A view of the 1993-1994 California Current based on surface drifters, floats, and remotely sensed data, *J. Geophys. Res.*, *105*(C4), 8575–8604.

Castelao, R. M., and J. A. Barth (2005), Coastal ocean response to summer upwelling favorable winds in a region of alongshore bottom topography variations off Oregon, *J. Geophys. Res.*, *110*, C10S04, doi:10.1029/2004JC002409.

Castelao, R. M., T. P. Mavor, J. A. Barth, and L. C. Breaker (2006), Sea surface temperature fronts in the California Current System from geostationary satellite observations, *J. Geophys. Res.*, *111*, C09026, doi:10.1029/2006JC003541.

Chelton, D. B., M. G. Schlax, R. M. Samelson, and R. A. de Szoeke (2007), Global observations of large oceanic eddies, *Geophys. Res. Lett.*, *34*, L15606, doi:10.1029/2007GL030812.

Chereskin, T. K., M. Y. Morris, P. P. Niiler, P. M. Kosro, R. L. Smith, S. R. Ramp, C. A. Collins, and D. L. Musgrave (2000), Spatial and temporal characteristics of the mesoscale circulation of the California Current from eddy-resolving moored and shipboard measurements, *J. Geophys. Res.*, *105*(C1), 1245–1269.

Collins, C. A., C. G. Castro, H. Asanuma, T. A. Rago, S.-K. Han, R. Durazo, and F. P. Chavez (2002), Changes in the hydrography of Central California waters associated with the 1997-98 El Nino, *Prog. Oceanogr.*, *54*, 129–147.

Collins, C. A., L. M. Ivanov, O. V. Melnichenko, and N. Garfield (2004), California Undercurrent variability and eddy transport estimated from RAFOS float observations, *J. Geophys. Res.*, *109*, C05028, doi:10.1029/2003JC002191.

Cornuelle, B. D., T. K. Chereskin, P. P. Niiler, M. Y. Morris, and D. L. Musgrave (2000), Observations and modeling of a California undercurrent eddy, *J. Geophys. Res.*, *105*(C1), 1227–1243.

Crawford, W. R., J. Y. Cherniawsky, and M. G. G. Foreman (2000), Multi-year meanders and eddies in the Alaskan Stream as observed by TOPEX/POSEIDON altimeter, *Geophys. Res. Lett.*, *27*(7), 1025–1028.

Durazo, R., and T. R. Baumgartner (2002), Evolution of oceanographic conditions off Baja California: 1997–1999, *Prog. Oceanogr.*, *54*, 7–31.

Farge, M. (1992), Wavelet transforms and their applications to turbulence, *Annu. Rev. Fluid Mech.*, *24*, 395–457.

Haidvogel, D. B., A. Beckmann, and K. S. Hedstrom (1991), Dynamical simulations of filament formation and evolution in the coastal transition zone, *J. Geophys. Res.*, *96*(C8), 15,017–15,040.

Henson, S. A., and A. C. Thomas (2007a), Interannual variability in timing of bloom initiation in the California Current System, *J. Geophys. Res.*, *112*, C08007, doi:10.1029/2006JC003960.

Henson, S. A., and A. C. Thomas (2007b), Phytoplankton scales of variability in the California Current System: 1. Interannual and cross-shelf variability, *J. Geophys. Res.*, *112*, C07017, doi:10.1029/2006JC004039.

Hickey, B. M., R. E. Thomson, H. Yih, and P. H. LeBlond (1991), Velocity and temperature fluctuations in a buoyancy-driven current off Vancouver Island, *J. Geophys. Res.*, *96*(C6), 10,507–10,538.

Holland, C. L., and G. T. Mitchum (2001), Propagation of Big Island eddies, *J. Geophys. Res.*, *106*(C1), 935–944.

Hooff, R. C., and W. T. Peterson (2006), Copepod biodiversity as an indicator of changes in ocean and climate conditions of the northern California current ecosystem, *Limnol. Oceanogr.*, *51*(6), 2607–2620.

Hormazabal, S., G. Shaffer, and O. Leth (2004), Coastal transition zone off Chile, *J. Geophys. Res.*, *109*, C01021, doi:10.1029/2003JC001956.

Huyer, A., J. A. Barth, P. M. Kosro, R. K. Shearman, and R. L. Smith (1998), Upper-ocean water mass characteristics of the California current, summer 1993, *Deep Sea Res., Part II*, *45*(8–9), 1411–1442.

Huyer, A., R. L. Smith, and J. Fleischbein (2002), The coastal ocean off Oregon and Northern California during the 1997–8 El Niño, *Prog. Oceanogr.*, *54*, 311–341.

Huyer, A., P. A. Wheeler, P. T. Strub, R. L. Smith, R. Letelier, and P. M. Kosro (2007), The Newport line off Oregon—Studies in the North East Pacific, *Prog. Oceanogr.*, *75*, 126–160.

Ikeda, M., and W. J. Emery (1984), Satellite observations and modeling of meanders in the California Current system, *J. Phys. Oceanogr.*, *14*, 1434–1450.

Kelly, K., R. Beardsley, R. Limeburner, K. Brink, J. Paduan, and T. Chereskin (1998), Variability of the near-surface eddy kinetic energy in the California Current based on altimetric, drifter, and moored current data, *J. Geophys. Res.*, *103*(C6), 13,067–13,083.

Kosro, P. M. (2002), A poleward jet and an equatorward undercurrent observed off Oregon and northern California during the 1997–98 El Niño, *Prog. Oceanogr.*, *54*, 343–360.

Kosro, P. M., and A. Huyer (1986), CTD and velocity surveys of seaward jets off northern California, July 1981 and 1982, *J. Geophys. Res.*, *91*(C6), 7680–7690.

Kosro, P., et al. (1991), The structure of the transition zone between coastal waters and the open ocean off northern California, winter and spring 1987, *J. Geophys. Res.*, *96*(C8), 4707–4730.

Kosro, P. M., W. T. Peterson, B. M. Hickey, R. K. Shearman, and S. D. Pierce (2006), Physical versus biological spring transition: 2005, *Geophys. Res. Lett.*, *33*, L22S03, doi:10.1029/2006GL027072.

Lagerloef, G. S. E. (1992), The Point Arena Eddy: A recurring summer anticyclone in the California Current, *J. Geophys. Res.*, *97*(C8), 12,557–12,568.

Legaard, K. R., and A. C. Thomas (2006), Spatial patterns in seasonal and interannual variability of chlorophyll and sea surface temperature in the California Current, *J. Geophys. Res.*, *111*, C06032, doi:10.1029/2005JC003282.

Legaard, K. R., and A. C. Thomas (2008), Spatial patterns of intraseasonal variability of chlorophyll and sea surface temperature in the California Current, *J. Geophys. Res.*, *112*, C09006, doi:10.1029/2007JC004097.

Le Traon, P. Y., Y. Faugere, F. Hernandez, J. Dorandeu, F. Mertz, and M. Ablain (2003), Can we merge GEOSAT Follow-On with TOPEX/POSEIDON and ERS-2 for an improved description of the ocean circulation?, *J. Atmos. Oceanic Technol.*, *20*(6), 889–895.

Mackas, D. L., and K. O. Coyle (2005), Shelf-offshore exchange processes, and their effects on mesozooplankton biomass and community composition patterns in the northeast Pacific, *Deep Sea Res., Part II*, *52*, 707–725.

Mackas, D. L., L. Washburn, and S. L. Smith (1991), Zooplankton community pattern associated with a California Current cold filament, *J. Geophys. Res.*, *96*(C8), 14,781–14,797.

Mantua, N. J., S. R. Hare, Y. Zhang, J. M. Wallace, and R. C. Francis (1997), A Pacific interdecadal climate oscillation with impacts on salmon production, *Bull. Am. Meteorol. Soc.*, *78*, 1069–1079.

Marchesiello, P., J. C. McWilliams, and A. Shchepetkin (2003), Equilibrium structure and dynamics of the California Current System, *J. Phys. Oceanogr.*, *33*(4), 755–783.

McPhaden, M. J. (1999), Genesis and evolution of the 1997–98 El Niño., *Science*, *283*, 950–954.

Melsom, A., S. D. Meyers, H. E. Hurlburt, E. J. Metzger, and J. J. O'Brien (1999), ENSO effects on Gulf of Alaska eddies, *Earth Interact.*, *3*(1), 1.

Melsom, A., E. J. Metzger, and H. E. Hurlburt (2003), Impact of remote oceanic forcing on Gulf of Alaska sea levels and mesoscale circulation, *J. Geophys. Res.*, *108*(C11), 3346, doi:10.1029/2002JC001742.

Meyers, S. D., B. G. Kelly, and J. J. O'Brien (1993), An introduction to wavelet analysis in oceanography and meteorology: With application to the dispersion of Yanai Waves, *Mon. Weather Rev.*, *121*, 2858–2866.

Miller, A. J., and N. Schneider (2000), Interdecadal climate regime dynamics in the North Pacific Ocean: Theories, observations and ecosystem impacts, *Prog. Oceanogr.*, *47*, 355–379.

Narimousa, S., and T. Maxworthy (1989), Application of a laboratory model to the interpretation of satellite and field observations of coastal upwelling, *Dyn. Atmos. Oceans*, *13*(1), 1–146.

Palacios, D. M., S. J. Bograd, D. G. Foley, and F. B. Schwing (2006), Oceanographic characteristics of biological hot spots in the North Pacific: A remote sensing perspective, *Deep Sea Res., Part II*, *53*, 250–269.

Pascual, A., Y. Faugère, G. Larnicol, and P.-Y. L. Traon (2006), Improved description of the ocean mesoscale variability by combining four satellite altimeters, *Geophys. Res. Lett.*, *33*, L02611, doi:10.1029/2005GL024633.

Percival, D. B., and A. T. Walden (2000), *Wavelet Methods for Time Series Analysis*, 594 pp., Cambridge Univ. Press, New York.

Pierce, S. D., J. A. Barth, R. E. Thomas, and G. W. Fleischer (2006), Anomalously warm July 2005 in the northern California Current: Historical context and the significance of cumulative wind stress, *Geophys. Res. Lett.*, *33*, L22S04, doi:10.1029/2006GL027149.

Powell, T. M., C. V. W. Lewis, E. N. Curchitser, D. B. Haidvogel, A. J. Hermann, and E. L. Dobbins (2006), Results from a three-dimensional, nested biological-physical model of the California Current System and comparisons with statistics from satellite imagery, *J. Geophys. Res.*, *111*, C07018, doi:10.1029/2004JC002506.

Schwing, F. B., T. Murphree, L. deWitt, and P. M. Green (2002a), The evolution of oceanic and atmospheric anomalies in the northeast Pacific during the El Niño and La Niña events of 1995–2001, *Prog. Oceanogr.*, *54*, 459–491.

Schwing, F. B., T. Murphree, and P. M. Green (2002b), The Northern Oscillation Index (NOI): A new climate index for the northeast Pacific, *Prog. Oceanogr.*, *53*, 115–139.

Schwing, F. B., N. A. Bond, S. J. Bograd, T. Mitchell, M. A. Alexander, and N. Mantua (2006), Delayed coastal upwelling along the U. S. West Coast in 2005: A historical perspective, *Geophys. Res. Lett.*, *33*, L22S01, doi:10.1029/2006GL026911.

Snyder, M. A., L. C. Sloan, N. S. Diffenbaugh, and J. L. Bell (2003), Future climate change and upwelling in the California Current, *Geophys. Res. Lett.*, *30*(15), 1823, doi:10.1029/2003GL017647.

Strub, P. T., and C. James (2000), Altimeter-derived variability of surface velocities in the California Current System: 2. Seasonal circulation and eddy statistics, *Deep Sea Res., Part II*, *47*, 831–870.

Strub, P. T., and C. James (2002a), Altimeter-derived surface circulation in the large-scale NE Pacific Gyres, *Part 1. Seasonal variability, Prog. Oceanogr.*, *53*, 163–183.

Strub, P. T., and C. James (2002b), Altimeter-derived surface circulation in the large-scale NE Pacific Gyres. Part 2: 1997–1998 El Niño anomalies, *Prog. Oceanogr.*, *53*, 185–214.

Strub, P. T., and C. James (2003), Altimeter estimates of anomalous transports into the northern California Current during 2000-2002, *Geophys. Res. Lett.*, *30*(15), 8025, doi:10.1029/2003GL017513.

Strub, P. T., P. M. Kosro, and A. Huyer (1991), The nature of the cold filaments in the California Current System, *J. Geophys. Res.*, *96*(C8), 14,743–14,768.

Torrence, C., and G. P. Compo (1998), A practical guide to wavelet analysis, *Bull. Am. Meteorol. Soc.*, *79*, 61–78.

Wilkin, J. L., M. M. Bowen, and W. J. Emery (2002), Mapping mesoscale currents by optimal interpolation of satellite radiometer and altimeter data, *Ocean Dyn.*, *52*, 95–103.

Zamudio, L., A. P. Leonardi, S. D. Meyers, and J. J. O'Brien (2001), ENSO and eddies on the southwest coast of Mexico, *Geophys. Res. Lett.*, *28*(1), 13–16.

J. E. Keister and P. T. Strub, College of Oceanic and Atmospheric Sciences, Oregon State University, 104 COAS Administration Building, Corvallis, OR 97331, USA. (jkeister@coas.oregonstate.edu)